

Title here

Elio Campitelli * and Leandro Díaz

CIMA UBA blablabla

Carolina Vera

⁵ **Corresponding author:* Elio Campitelli, elio.campitelli@cima.fcen.uba.ar

ABSTRACT

6 Enter the text of your abstract here. This is a sample American Meteorological Society (AMS)
7 \LaTeX template. This document provides authors with instructions on the use of the AMS \LaTeX tem-
8 plate. Authors should refer to the file `amspaper.tex` to review the actual \LaTeX code used to create
9 this document. The `template.tex` file should be modified by authors for their own manuscript.

10 *Significance statement.* This is significant because I wrote it.

11 **1. Introduction**

12 yada yada SAM yada yada circulation.. yada yada so important. yada yada many impacts.

13 **2. Methods**

14 **1) DATA**

15 We used monthly geopotential height at 2.5 longitude by 2.5 latitude resolution from ERA5
16 (Hersbach et al.) for the period 1979 to 2018 (inclusive).

17 Monthly temperature NOAA Global Surface Temperature (NOAAGlobalTemp) 5.0 degree lati-
18 tude x 5.0 degree longitude global grid (Vose et al. 2012; Smith et al. 2008). The same analysis
19 was carried out using CRUTEM4 (Osborn and Jones 2014) (not shown).

20 We used monthly precipitation data from CPC Merged Analysis of Precipitation (Xie and Arkin
21 1997) 2.5 degree latitude x 2.5 degree longitude.

22 **2) DEFINITION OF INDICES**

23 We defined the Southern Annular Mode (SAM) as the leading EOF of the monthly anomalies of
24 geopotential field at 700 hPa south of 20°S (citation?). The EOF was performed by computing the
25 Singular Value Decomposition of the data matrix consisting in 481 rows and 4176 columns (144
26 points of longitude and 29 points of latitude). The values were weighted by the square root of the
27 cosine of latitude to account for the non-equal area of each gridpoint (Chung and Nigam 1999).
28 This same method was used at the rest of the levels considered in this paper.

29 To separate between the zonally symmetric and asymmetric components of the SAM, we com-
30 puted the zonal mean and anomalies of the full SAM spatial pattern. The results are shown in

31 Figure 3 for 700hPa. The full spatial signal ($\text{EOF}_1(\lambda, \phi)$) is the sum of the zonally asymmetric
32 ($\text{EOF}_1^*(\lambda, \phi)$) and symmetric ($[\text{EOF}_1](\lambda, \phi)$) components. We then compute the “Full”, “Asym-
33 metric” and “Symmetric” indices, by regressing each geopotential field on these patterns (weighting
34 by the cosine of latitude).

35 The three indices are normalised by dividing them by the standard deviation of the “Full” index
36 at each level. This means that comparing the magnitude between indices is meaningful, but it also
37 means that not every index will have unit standard deviation.

38 3) SIGNIFICANCE

39 We adjusted p-values for False Detection Rate following Wilks (2016).

40 3. Results

41 a. *Temporal evolution*

42 Figure 4 shows the resulting Asymmetric and Symmetric time series corresponding to 700 and
43 30hPa. #FIXME

44 At first glance the series can be distinguished by their distributions. Whereas the tropospheric
45 indices are approximately normally distributed, the stratospheric indices are more long-tailed; that
46 is, extreme values (both negative and positive) abound. The Asymmetric series have both more
47 variability in the higher frequencies than the Symmetric series.

48 The stratospheric Symmetric SAM varies strongly with a two-year period, which can be seen
49 using spectral methods (Figure A3) or in the autocorrelation structure (Figure A4). There is a
50 local peak at 2 years in the periodogram of the tropospheric Symmetric SAM also, although it's not
51 statistically significant. In the troposphere the most significant peak of variability is found in the
52 Asymmetric index at around 3.6 months.

Correlations between the Asymmetric and Symmetric series are constant through the troposphere, fluctuating between 0.39 and 0.45 (Figure 5). Furthermore, the cross-correlation of each series across levels –shown in Figure 6– are high in the troposphere (greater than 0.9) for both indices. This suggests that both the Asymmetric and the Symmetric component of the tropospheric SAM are highly vertically coherent, both in their individual evolution and their temporal relationship. This is to be expected since the SAM is mostly equivalent barotropic (citaaaa).

In the stratosphere the situation is different. As can be seen in Figure 5, the relationship between the Asymmetric and Symmetric indices varies with height above 100 hPa. It starts to decrease right over the tropopause, reaches a minimum of 0.21 at 20 hPa and then it increases again monotonically with height up to the uppermost level of the reanalysis. The cross-correlation across levels in the stratosphere is generally weaker than in the troposphere (Figure 6). Furthermore, above 100 hPa, the cross-correlation decreases more rapidly with height for the Symmetric SAM than for the Asymmetric SAM as evidenced by the wider dark red areas near the diagonal in Figure 6b) vs. Figure 6c). Moreover, the stratospheric Symmetric SAM seems to be slightly more connected to the troposphere than the Asymmetric SAM; this can be seen by the lower correlation values in the top right quadrant of Figure 6b) in comparison with Figure 6c).

Figure 6a) show the cross-correlation across levels for the Full, Symmetric and Asymmetric SAM indices. The high values below 100 hPa in panel a) reflect the vertical (zero-lag) coherence of the tropospheric SAM. Above 100 hPa correlation between levels falls off rapidly, indicating less coherent (zero-lag) variability. At the same time, there is a non negligible correlation between the troposphere and the lower-to-middle stratosphere. By examining panels b and c we see that the Asymmetric and Symmetric SAM share the same high level of coherence in the troposphere but that the Asymmetric SAM is relatively more coherent in the stratosphere. The tropospheric-stratospheric connection is only present in the Symmetric SAM.

77 Figure 7 shows normalised decadal trends for each index for the whole period along with a 95%
78 interval in shading. There is a statistically significant increase in positive SAM in the troposphere
79 (panel a), which has been already documented in other studies (e.g. Fogt and Marshall (2020)).
80 Panels b and c of Figure 7 show that this increase is evident only in the Symmetric component.
81 This distinction should prove useful when attributing trends in other variables such as temperature
82 and precipitation to trends in the SAM.

83 *b. Spatial patterns*

84 To understand the spatial patterns associated with both indices, we regressed monthly geopotential
85 anomalies into both indices using multiple regression (Figure A6 illustrates the difference between
86 computing two simple regressions and one multiple regression).

87 Figure 8 shows the spatial year-long regression for selected levels. In the troposphere the Full
88 annular mode is clearly “contaminated” with well known zonal asymmetries (panels g and j) which
89 are successfully separated by our methodology (panels h, i, k and l). In the stratosphere, the spatial
90 pattern associated with the Full SAM is much more clearly dominated by a zonally symmetric,
91 monopolar structure (panels a and d) that is, however, not perfectly centered in the south pole. The
92 monopoles obtained by multiple regression with the Asymmetric and Symmetric SAM (panels c
93 and f in Figure 8) is much more symmetric and the shift from total symmetry is captured by the
94 regression pattern of the Asymmetric SAM as a wave-1 pattern (panels b and e).

95 The amplitude of each zonal wave number at each latitude at 50 hPa and 700 hPa is shown in
96 Figure 9, where wave number zero represents the zonal mean. Comparing between rows, this Figure
97 quantifies the relatively clean separation between the zonally symmetric and zonally asymmetric
98 structures, as it is evident how the mixture of waves of the Full field (first row) is very similar to
99 the sum of the waves of the Asymmetric and Symmetric field (second and third row, respectively).

The second row of Figure 9 shows that the Asymmetric SAM is overwhelmingly dominated by wave 1 in the stratosphere (panel b), while in the stratosphere it is composed of zonal waves 3 to 1 in decreasing level of importance.

From Figure 8 it appears that the vertical structure of the Asymmetric SAM is equivalent barotropic in the troposphere but baroclinic in the stratosphere. Anomalies are centered in the same locations in the troposphere (panels h and k), but show westerly displacement in the stratosphere (panels l and e). This is expanded in Figure 10, which shows a vertical cross-section of the regression coefficient corresponding to the middle row of Figure 8, area-weighted averaged between 65 and 40 degrees South. Below 100 hPa, anomalies are completely vertical, while above they show an important westerly tilt with height.

c. Impacts

1) TEMPERATURE

Figure 1 shows regression coefficients of each index at 700 hPa with surface temperature for each trimester. It is evident that the Asymmetric and Symmetric SAM indices are associated with overall distinct temperature patterns which can be obscured when using the Full SAM index. The Symmetric SAM signal is weaker than the Asymmetric SAM, as evidenced by the relatively smaller and less statistically significant regression coefficients in row 3 of Figure 1 compared with row 2.

In DJF (column a), the strong negative signal in the tropical Pacific in panel a.1 is mostly associated with the Asymmetric component (panel a.2), as is it largely absent in the Symmetric component (panel a.3). Furthermore, the Asymmetric SAM is also associated with low temperature anomalies in the Indian ocean, but this signal is obscured by the Symmetric variability and thus lost in the Full SAM. Over the continents, the Asymmetric SAM is associated with negative temperature anomalies which, again, mostly disappear in the Full SAM regression.

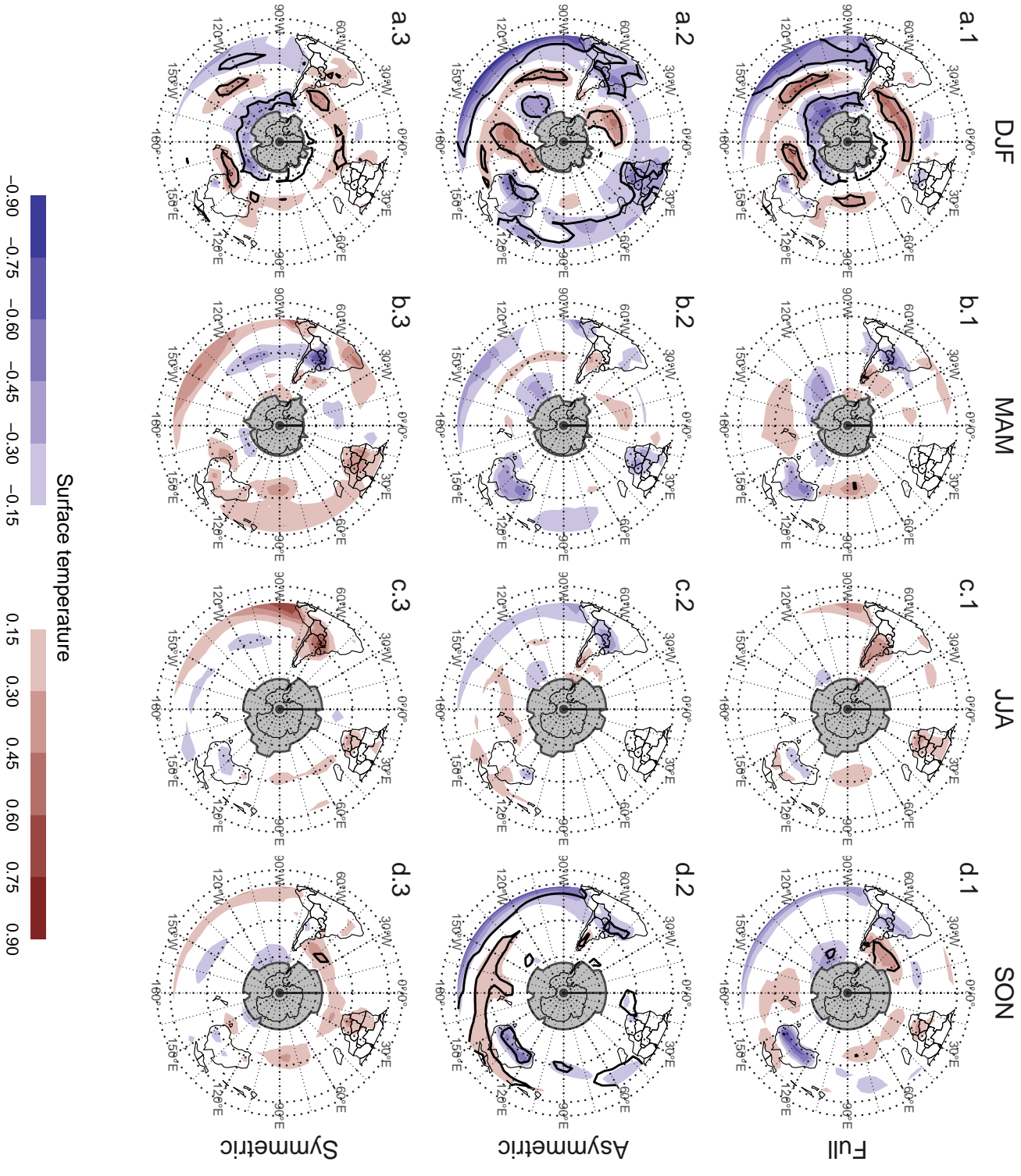


Fig. 1. Regression pattern of surface temperature with Asymmetric and Symmetric SAM. P-values smaller than 0.05 (controlling for False Detection Rate) as hatched areas. Gray areas have more than 15% of missing data.

The patterns seen in MAM and JJA (columns b and c) are not robustly significant in the sense that there are no areas with p-values below 0.05 when controlling for FDR following Wilks (2016). Nevertheless, it is interesting to note that in both trimesters, the sign of the regression is consistently flipped between the Asymmetric and Symmetric regressions. In South America, for example, the Asymmetric SAM is associated with positive temperature anomalies in MAM and negative temperature anomalies in JJA, while the opposite is the case for the Symmetric SAM.

Finally, in SON (column d), there is no significant temperature signal associated with the Symmetric SAM (panel d.3), while the Asymmetric SAM shows a relatively robust signal in the equatorial Pacific, Australia, and even Southeast South America. These strong signals are reduced in intensity in panel a.3.

2) PRECIPITATION

??

Acknowledgments. CMAP Precipitation data provided by the NOAA/OAR/ESRL PSL, Boulder, Colorado, USA, from their Web site at <https://psl.noaa.gov/>

NOAA Global Surface Temperature (NOAAGlobalTemp) data provided by the NOAA/OAR/ESRL PSL, Boulder, Colorado, USA, from their Web site at <https://psl.noaa.gov/>

References

Chung, C., and S. Nigam, 1999: Weighting of geophysical data in Principal Component Analysis. *Journal of Geophysical Research: Atmospheres*, **104 (D14)**, 16 925–16 928, doi: 10.1029/1999JD900234.

Fogt, R. L., and G. J. Marshall, 2020: The Southern Annular Mode: Variability, trends, and climate impacts across the Southern Hemisphere. *WIREs Climate Change*, **11 (4)**, e652, doi:

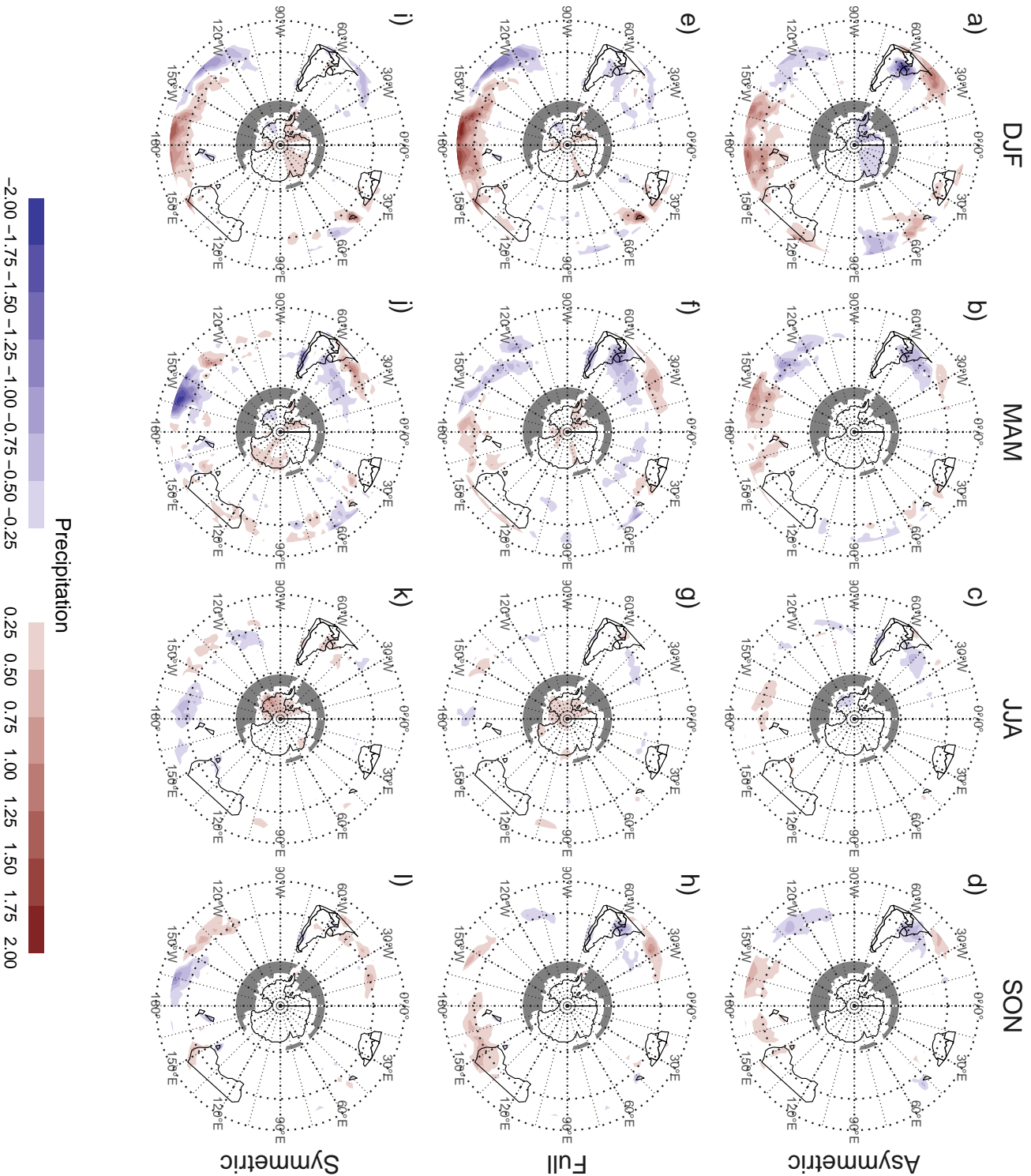


FIG. 2. Regression pattern of precipitation with Asymmetric and Symmetric SAM. P-values smaller than 0.05 (controlling for False Detection Rate)

10.1002/wcc.652.

Hersbach, H., and Coauthors, 2015: The ERA5 global reanalysis. *Quarterly Journal of the Royal Meteorological Society*, **n/a (n/a)**, doi:10.1002/qj.3803.

Osborn, T. J., and P. D. Jones, 2014: The CRUTEM4 land-surface air temperature data set: Construction, previous versions and dissemination via Google Earth. *Earth System Science Data*, **6 (1)**, 61–68, doi:10.5194/essd-6-61-2014.

Smith, T. M., R. W. Reynolds, T. C. Peterson, and J. Lawrimore, 2008: Improvements to NOAA’s Historical Merged Land–Ocean Surface Temperature Analysis (1880–2006). *J. Climate*, **21 (10)**, 2283–2296, doi:10.1175/2007JCLI2100.1.

Vose, R. S., and Coauthors, 2012: NOAA’s Merged Land–Ocean Surface Temperature Analysis. *Bull. Amer. Meteor. Soc.*, **93 (11)**, 1677–1685, doi:10.1175/BAMS-D-11-00241.1.

Wilks, D. S., 2016: “The Stippling Shows Statistically Significant Grid Points”: How Research Results are Routinely Overstated and Overinterpreted, and What to Do about It. *Bull. Amer. Meteor. Soc.*, **97 (12)**, 2263–2273, doi:10.1175/BAMS-D-15-00267.1.

Xie, P., and P. A. Arkin, 1997: Global Precipitation: A 17-Year Monthly Analysis Based on Gauge Observations, Satellite Estimates, and Numerical Model Outputs. *Bull. Amer. Meteor. Soc.*, **78 (11)**, 2539–2558, doi:10.1175/1520-0477(1997)078<2539:GPAYMA>2.0.CO;2.

APPENDIX

Extra figures

168	LIST OF FIGURES	
169	Fig. 1. Regression pattern of surface temperature with Asymmetric and Symmetric SAM	8
170	Fig. 2. Regression pattern of precipitation with Asymmetric and Symmetric SAM	10
171	Fig. 3. Spatial patterns of the first EOF of 700 hPa geopotential height	14
172	Fig. 4. Time series for the asymmetric SAM and symmetric SAM and density estimates	15
173	Fig. 5. Correlation between the Symmetric and Asymmetric SAM at each level	16
174	Fig. 6. Cross correlation between levels of the Full, Asymmetric and Symmetric SAM	17
175	Fig. 7. Trends for each index at each level	18
176	Fig. 8. Regression patterns of geopotential height at 30, 300 and 700 hPa with the Full, Asymmetric	
177	and Symmetric SAM	19
178	Fig. 9. Planetary wave amplitude for the regression patterns at 50 and 700 hPa	20
179	Fig. 10. Asymmetric coefficient of the multiple regression of mean monthly geopotential height	
180	anomalies between 65 and 40 South	21
181	Fig. A1. Lag-correlation between Symmetric and Asymmetric SAM at each level.	22
182	Fig. 11. Cross-correlation functions for each index and two different base levels	23
183	Fig. A3. Fourier spectrum of each timeseries. The shading indicates the 95% area derived by fitting	
184	an AR process to each series and bootstrapping 5000 simulated samples.	24
185	Fig. A4. Autocorrelation functions of each timeseries	25
186	Fig. A5. Regression pattern of precipitation with Asymmetric and Symmetric SAM. P-values smaller	
187	than 0.05 (controlling for False Detection Rate) as hatched areas.	26
188	Fig. A6. Regressions maps resulting from performing one multiple regression (column a) and from	
189	performing two simple regressions (column b)	27
190	Fig. A7. Zonal waves derived from the regression maps from performing one multiple regression	
191	(column a) and from performing two simple regressions (column b)	28
192	Fig. A8. Decadal trends of SAM indices for each season.	29

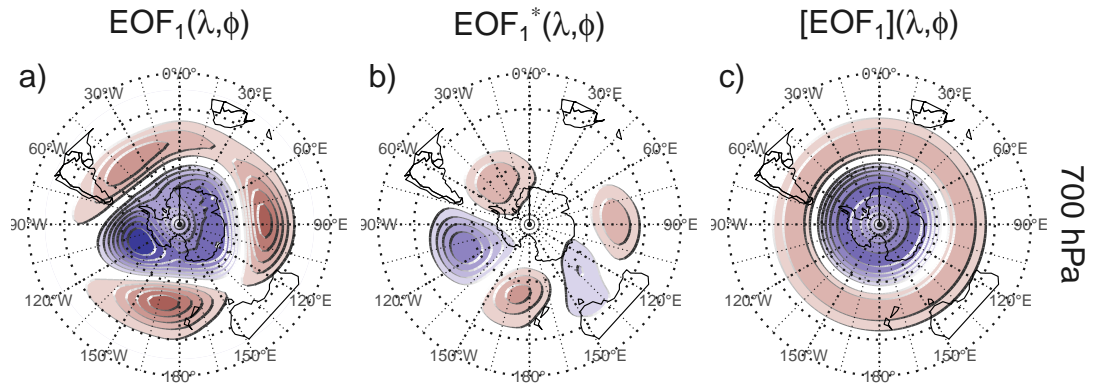


FIG. 3. Spatial patterns of the first EOF of 700 hPa geopotential height. Full field (left), zonally asymmetric component (middle) and zonally symmetric component (right). Arbitrary units.

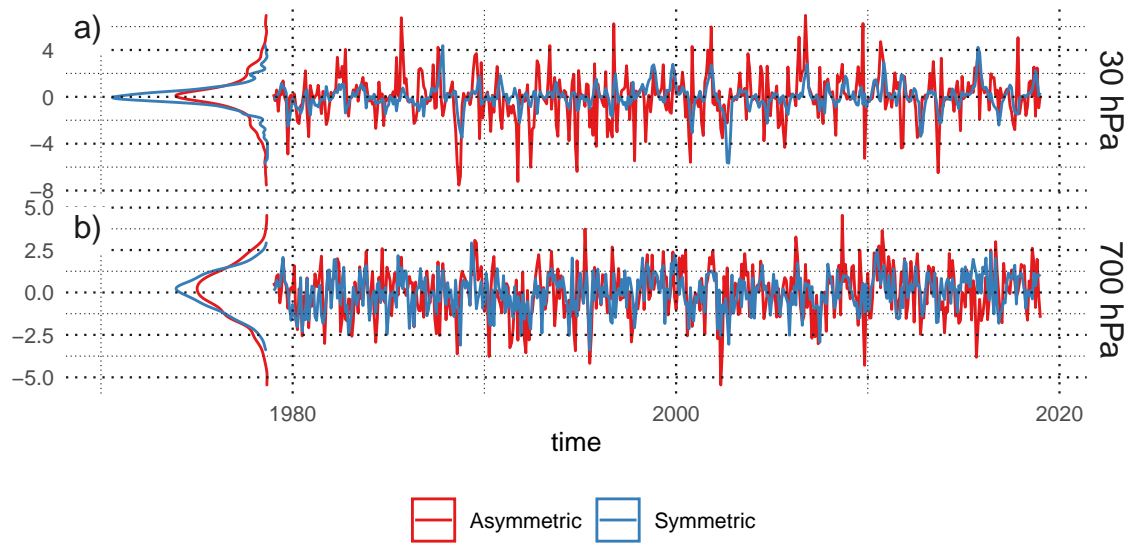


FIG. 4. Time series for the asymmetric SAM and symmetric SAM and density estimates.

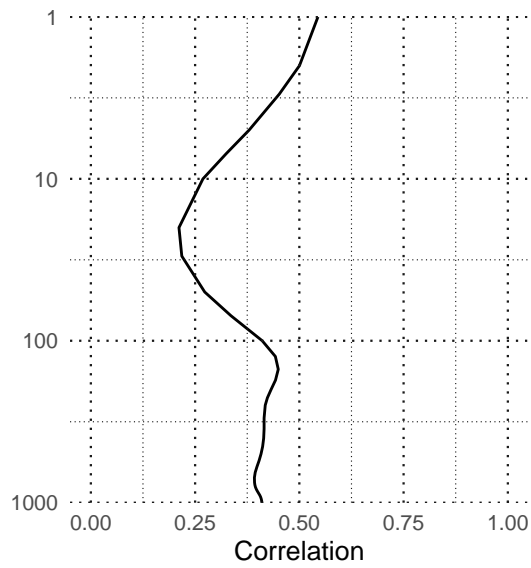


FIG. 5. Correlation between the Symmetric and Asymmetric SAM at each level.

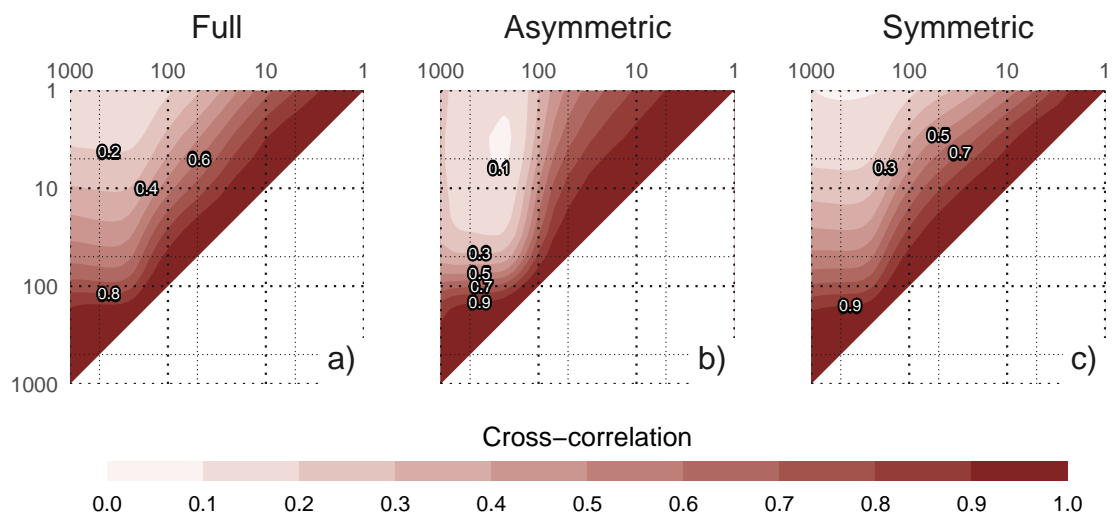


FIG. 6. Cross correlation between levels of the Full, Asymmetric and Symmetric SAM.

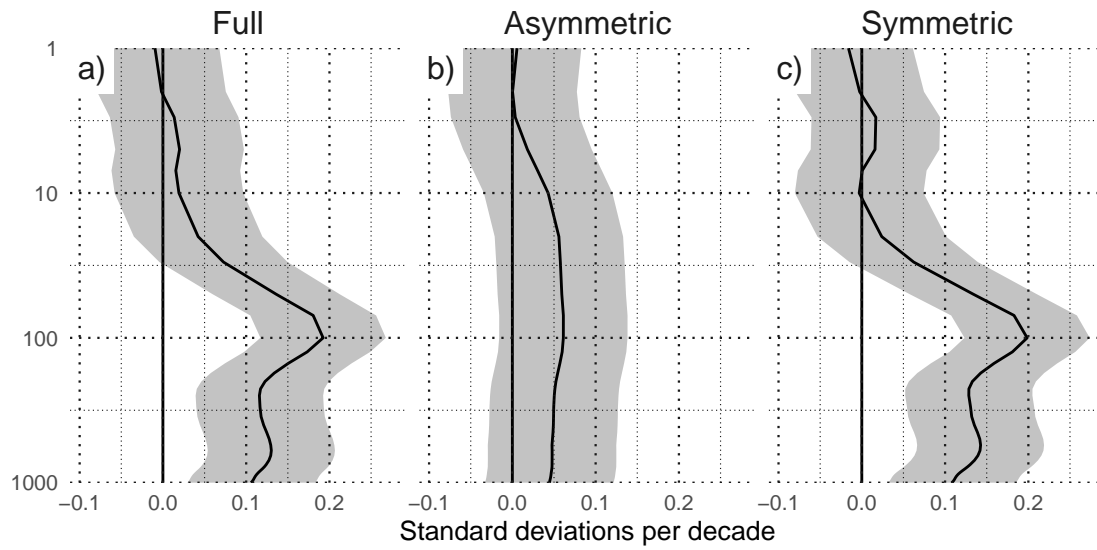


FIG. 7. Trends for each index at each level. Shading indicates the 95% confidence interval.

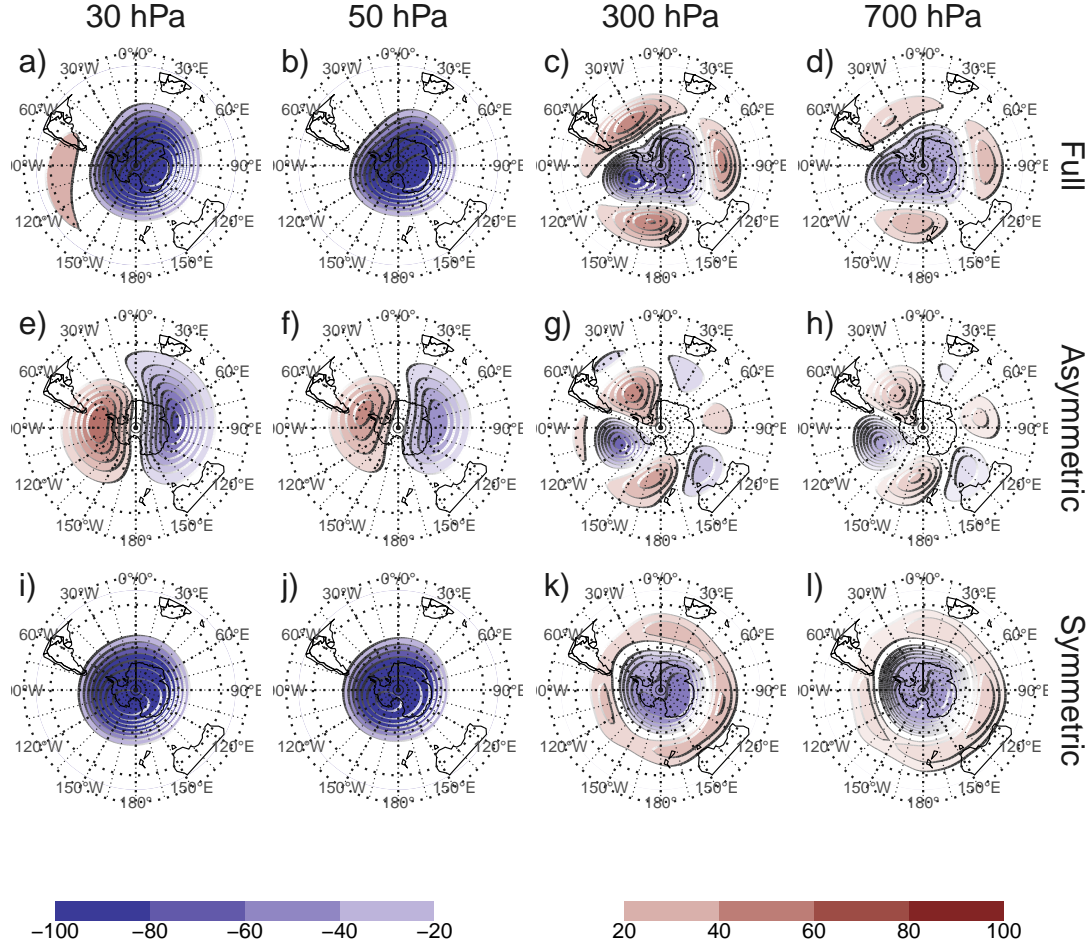


FIG. 8. Regression patterns of geopotential height at 30, 300 and 700 hPa with the Full, Asymmetric and Symmetric SAM. The regression patterns for Asymmetric and Symmetric SAM are the result of one multiple regression using both indices, not of two simple regressions involving each index by itself.

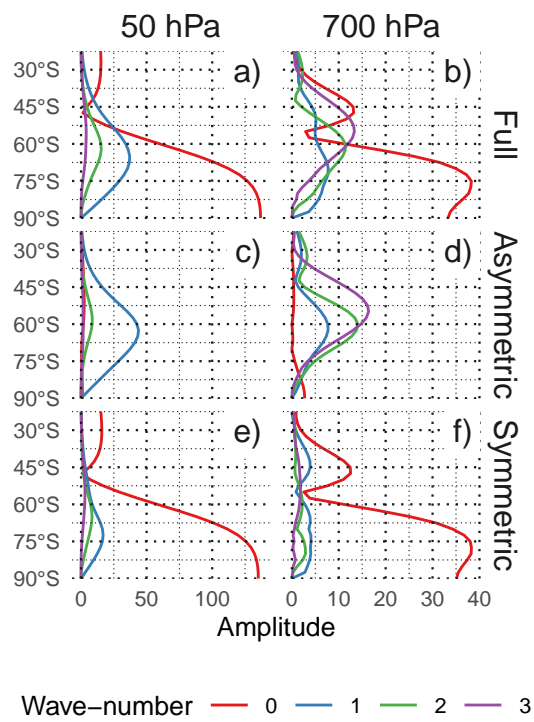


FIG. 9. Planetary wave amplitude for the regression patterns at 50 and 700 hPa.

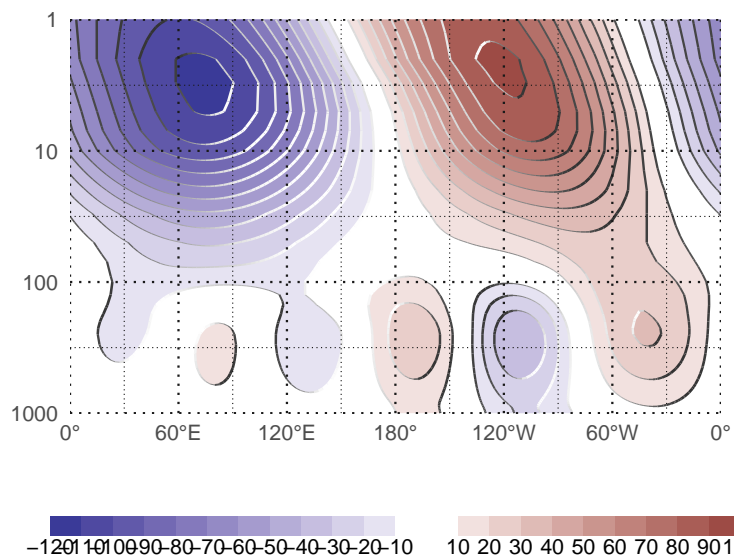


FIG. 10. Asymmetric coefficient of the multiple regression of mean monthly geopotential height anomalies
between 65 and 40 South. (this caption needs some love)

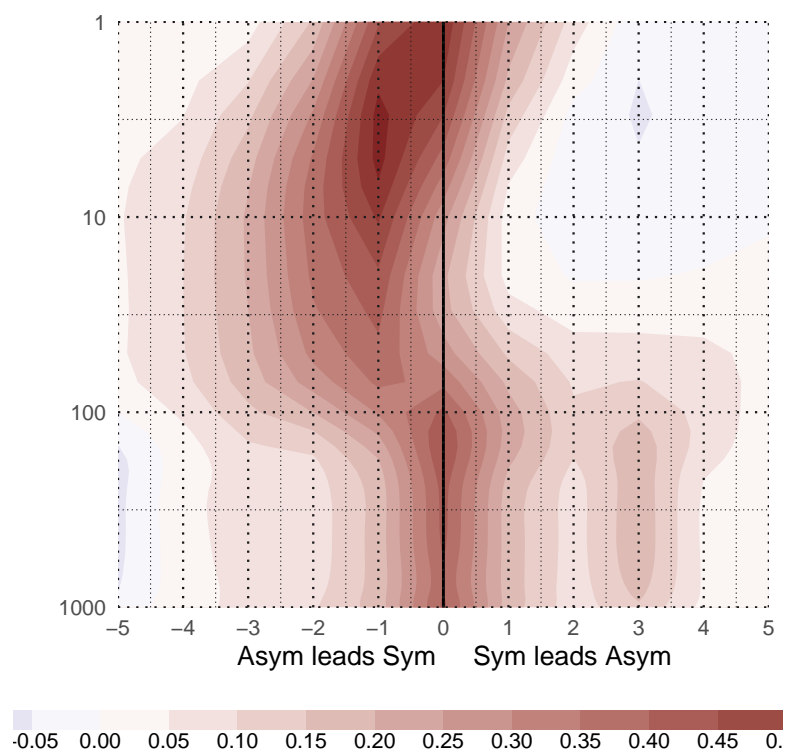


Fig. A1. Lag-correlation between Symmetric and Asymmetric SAM at each level.

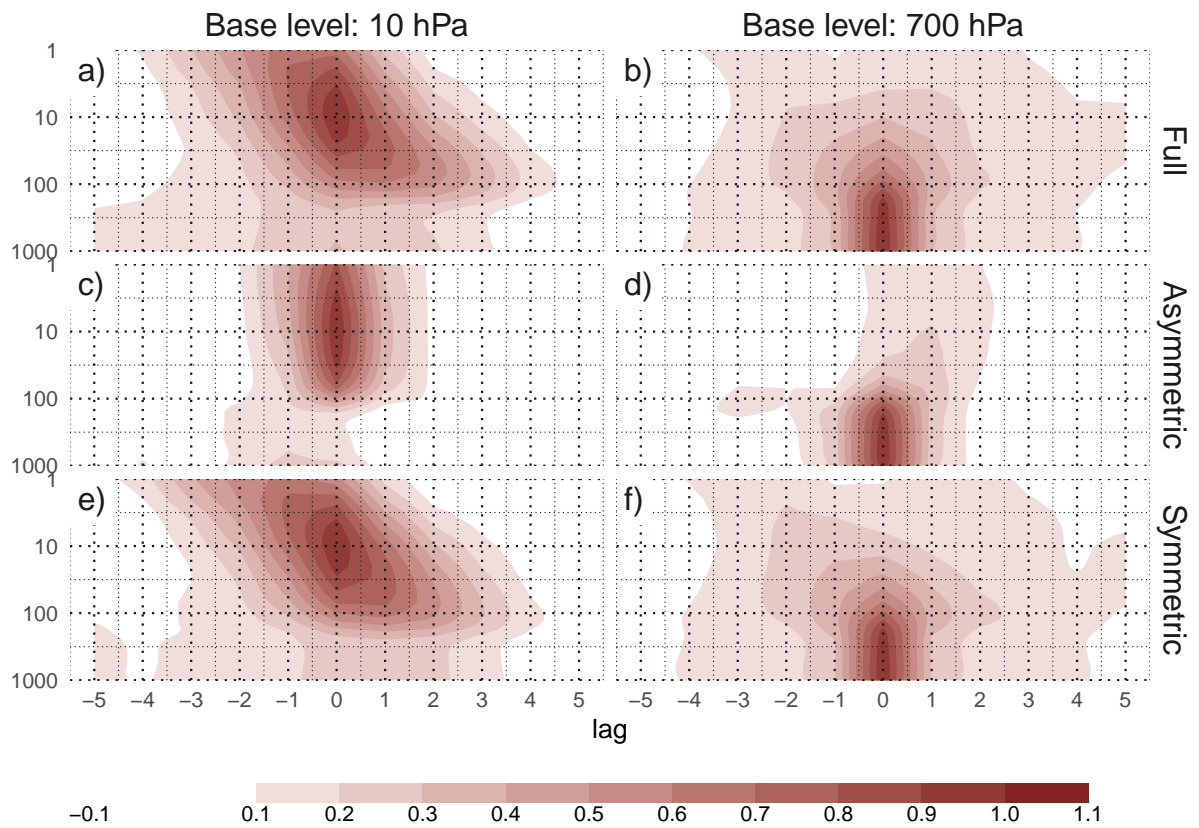


FIG. 11. Cross-correlation functions for each index and two different base levels.

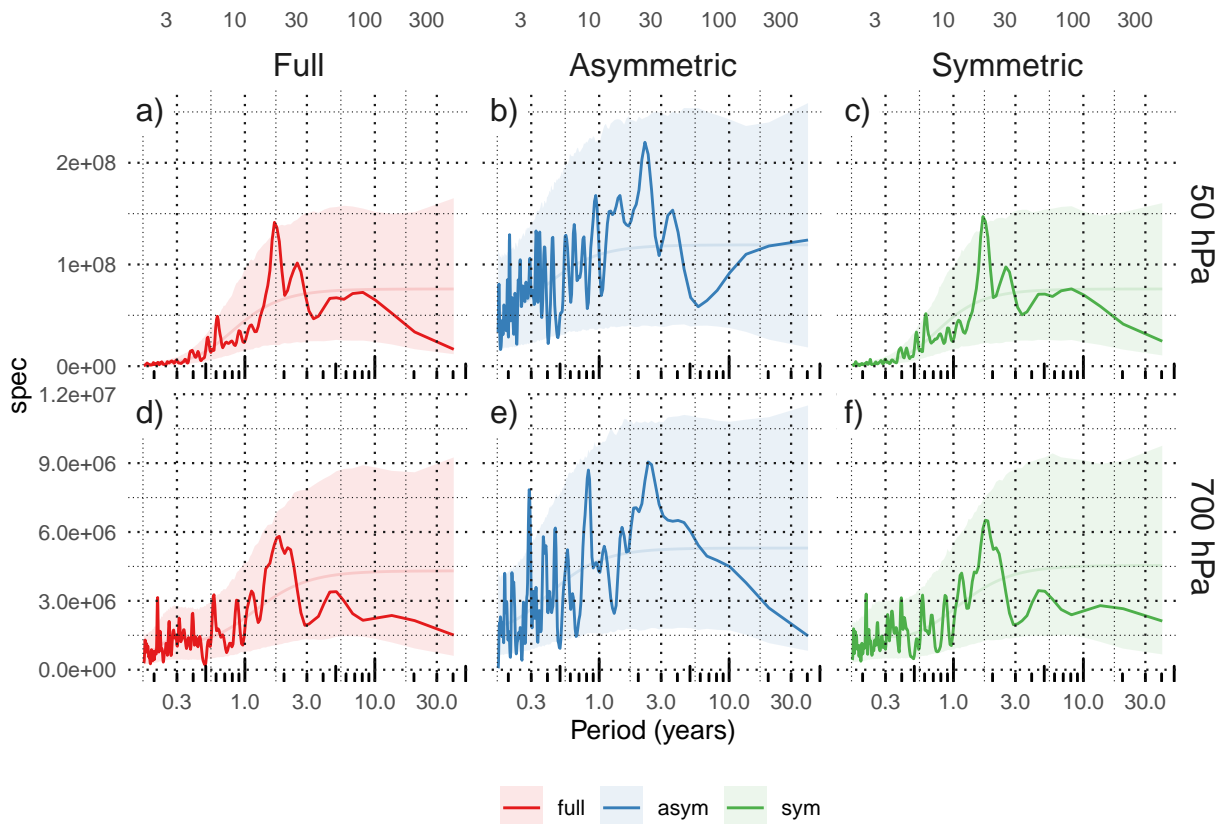


Fig. A3. Fourier spectrum of each timeseries. The shading indicates the 95% area derived by fitting an AR process to each series and bootstrapping 5000 simulated samples.

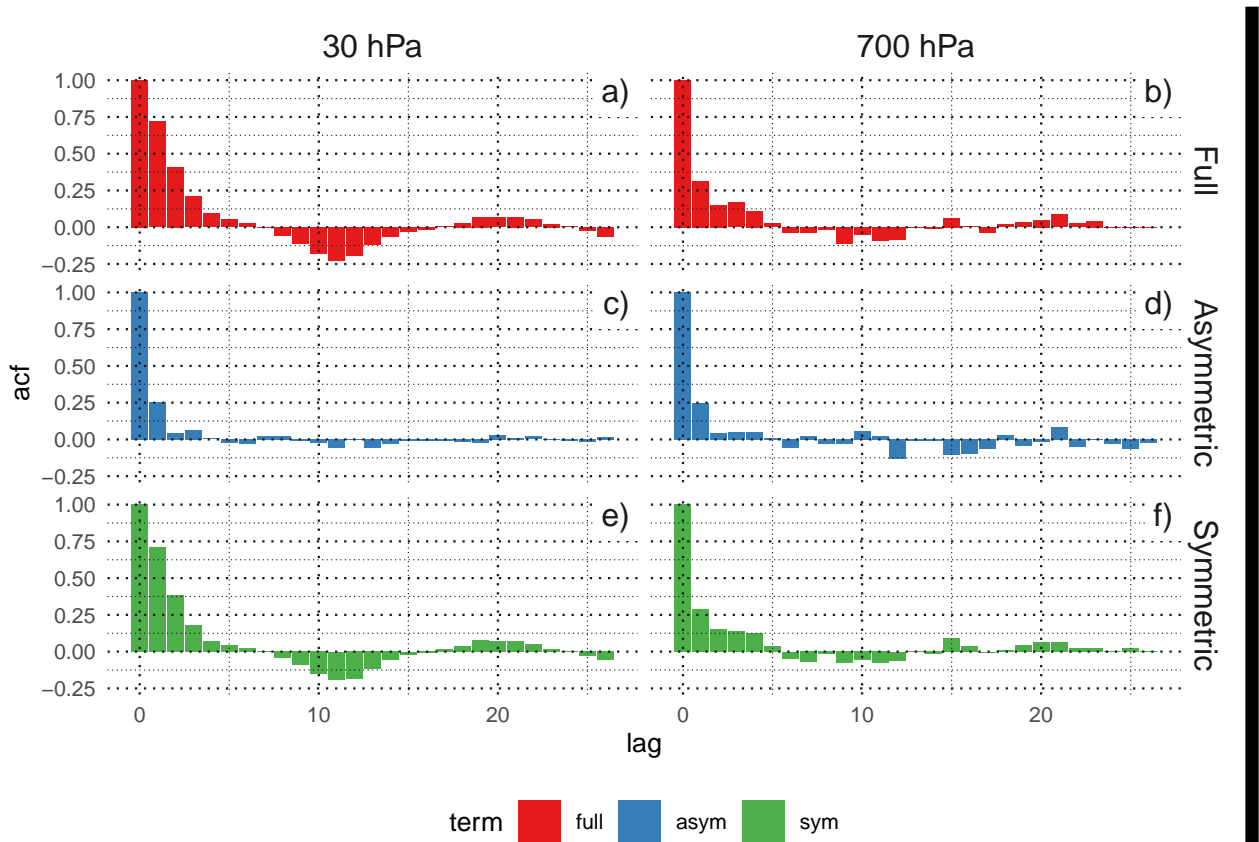


Fig. A4. Autocorrelation functions of each timeseries

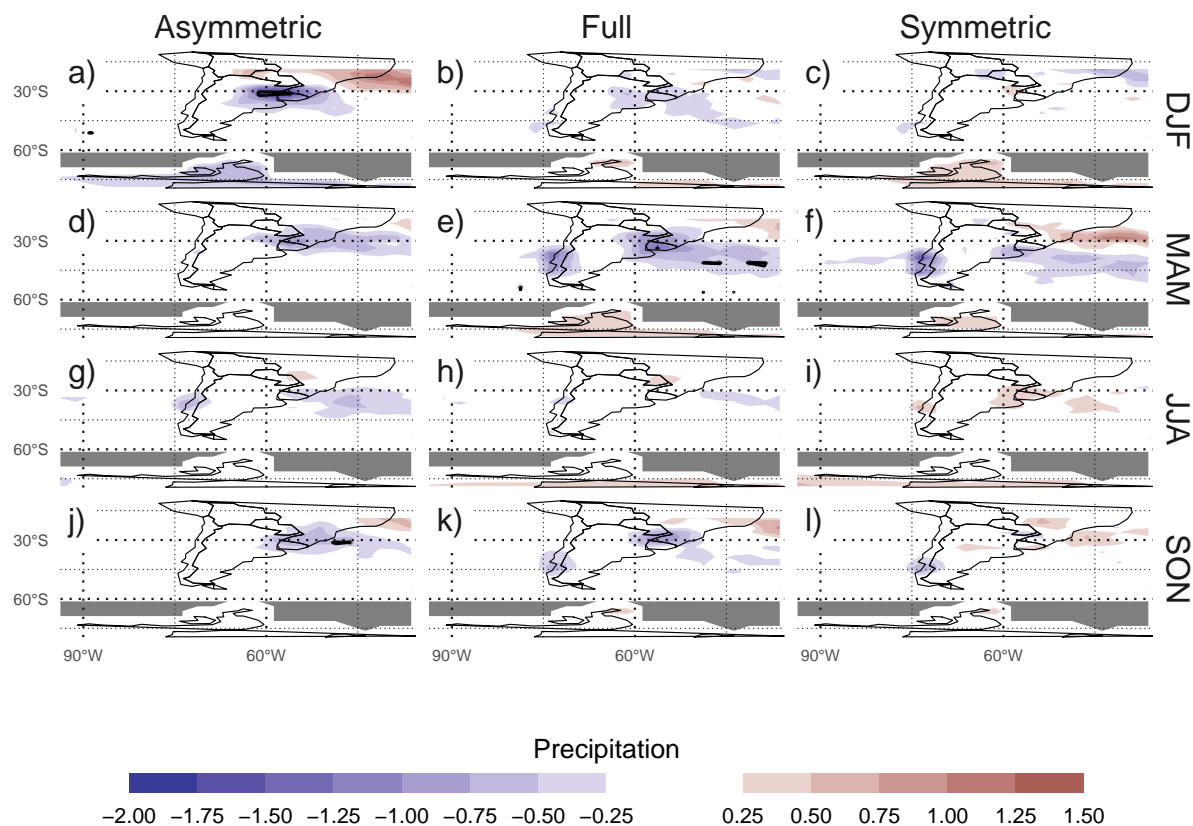
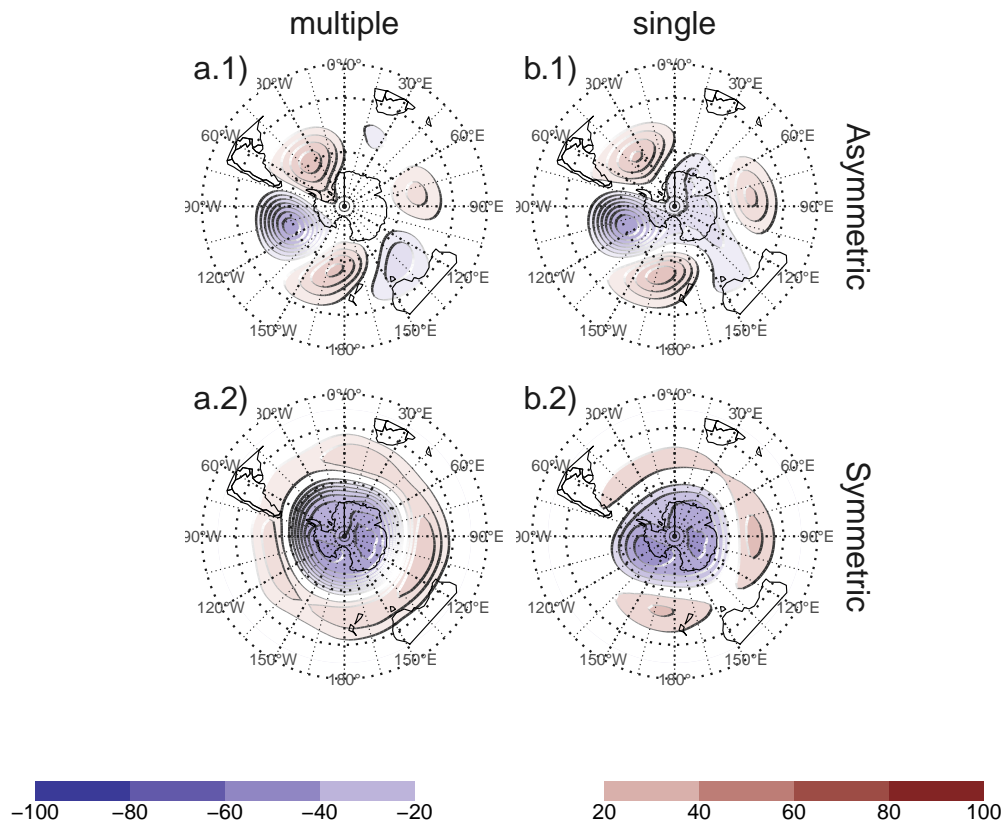
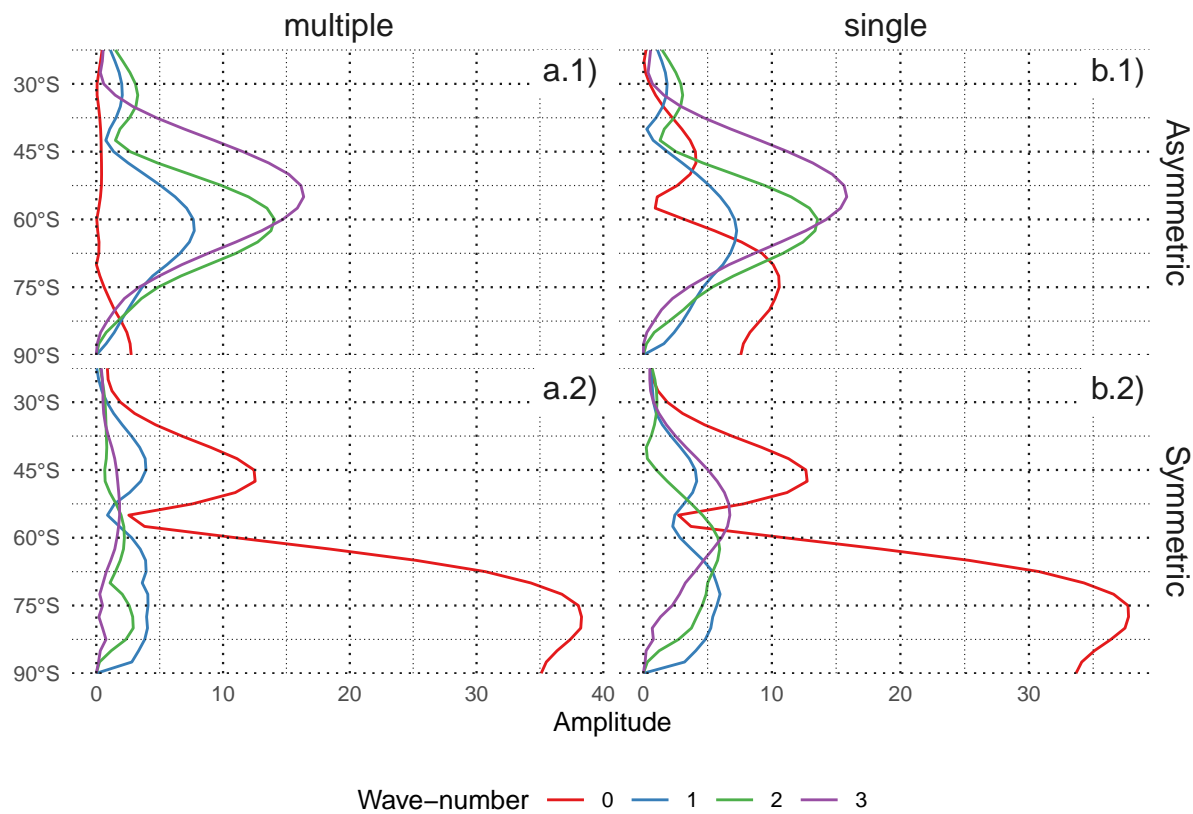


Fig. A5. Regression pattern of precipitation with Asymmetric and Symmetric SAM. P-values smaller than 0.05 (controlling for False Detection Rate) as hatched areas.



204 Fig. A6. Regressions maps resulting from performing one multiple regression (column a) and from performing
 205 two simple regressions (column b)



206 Fig. A7. Zonal waves derives from the regression maps from performing one multiple regression (column a)
 207 and from performing two simple regressions (column b)

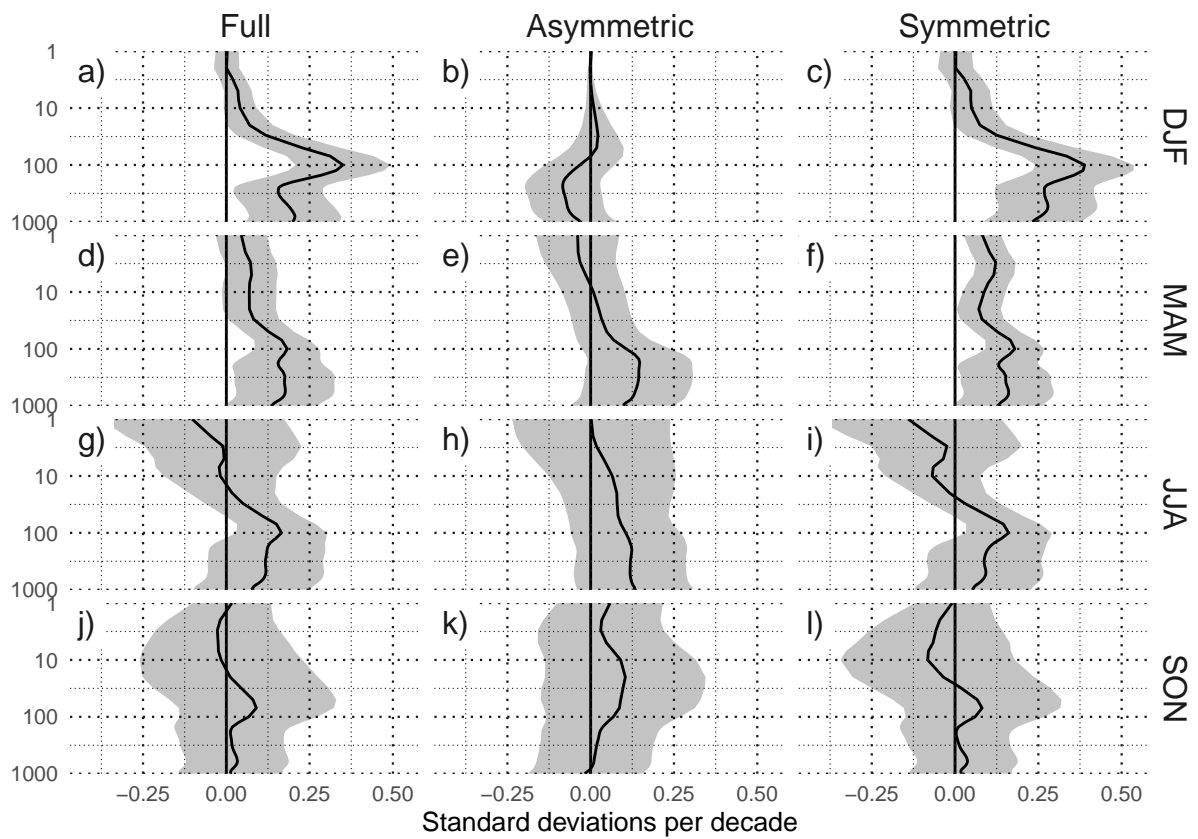


Fig. A8. Decadal trends of SAM indices for each season.